

REVIEW

An Invited Review for the Special 20th Anniversary Issue of MRMS

In vivo Human MR Spectroscopy Using a Clinical Scanner: Development, Applications, and Future Prospects

Moyoko Tomiyasu^{1,2} and Masafumi Harada^{3*}

MR spectroscopy (MRS) is a unique and useful method for noninvasively evaluating biochemical metabolism in human organs and tissues, but its clinical dissemination has been slow and often limited to specialized institutions or hospitals with experts in MRS technology. The number of 3-T clinical MR scanners is now increasing, representing a major opportunity to promote the use of clinical MRS. In this review, we summarize the theoretical background and basic knowledge required to understand the results obtained with MRS and introduce the general consensus on the clinical utility of proton MRS in routine clinical practice. In addition, we present updates to the consensus guidelines on proton MRS published by the members of a working committee of the Japan Society of Magnetic Resonance in Medicine in 2013. Recent research into multinuclear MRS equipped in clinical MR scanners is explained with an eye toward future development. This article seeks to provide an overview of the current status of clinical MRS and to promote the understanding of when it can be useful. In the coming years, MRS-mediated biochemical evaluation is expected to become available for even routine clinical practice.

Keywords: *clinical utility, magnetic resonance spectroscopy, metabolite, multi-nuclei*

Introduction

In vivo MR spectroscopy (MRS) was initially performed as phosphorus (³¹P)-MRS, which detects biochemical phosphorus compounds in tissue. These substances, which include adenosine triphosphate, phosphocreatine, and inorganic phosphate, participate in energy metabolism in viable cells, enabling researchers to observe dynamic changes in energy metabolism *in vivo* in specific settings using this technique. In the late 1980s, in the early stage of clinical MR instrumentation, some high-end clinical MRI machines were equipped with multinuclear systems including specific transmitter and receiver coils, and ³¹P-MRS could be used in

the clinical setting. However, owing to several disadvantages of this technique, including low sensitivity and complicated procedures for changing frequency and receivers, its clinical applications were strictly limited and the technique was not used in routine clinical practice.

Meanwhile, proton MRS (¹H-MRS) has been recognized as a useful method for evaluating cerebral metabolism that does not require a change in the frequency and receiver coils after brain MRI studies. Its targeted metabolites are several amino acids, lactate (Lac), creatine, and choline-containing compounds. In particular, n-acetyl aspartate (NAA) exhibits high levels in cerebral neurons. In the early 1990s, the characteristics of NAA were examined, with intense focus on its mechanisms and roles. This amino acid was found to be specific to neurons and to be synthesized through the direct acetylation of aspartate in mitochondria.¹ With NAA now considered a neuronal marker, ¹H-MRS subsequently started to receive more attention in clinical research and diagnosis than ³¹P-MRS. In clinical practice, ¹H-MRS is sometimes performed to investigate the levels of metabolites and provides additional information for the diagnostic process.

In this review, we focus on MRS performed using a clinical MR scanner, which is divided into three categories: (1) MRS with a clinical MR scanner, (2) the clinical utility of ¹H-MRS, and (3) the expected use of other nuclei besides protons in clinical MRS. Although we mainly use single-voxel ¹H-MRS in the brain to describe MRS, its principles

¹Department of Molecular Imaging and Theranostics, National Institutes for Quantum Science and Technology, Chiba, Chiba, Japan

²Department of Radiology, Kanagawa Children's Medical Center, Yokohama, Kanagawa, Japan

³Department of Radiology and Radiation Oncology, Graduate School of Biomedical Sciences, Tokushima University, Tokushima, Tokushima, Japan

*Corresponding author: Department of Radiology and Radiation Oncology, Graduate School of Biomedical Sciences, Tokushima University, 3-18-15, Kuramoto-cho, Tokushima, Tokushima 770-8503, Japan
Email: masafumi@tokushima-u.ac.jp



This work is licensed under a Creative Commons Attribution-NonCommercial-NoDerivatives International License.

©2022 Japanese Society for Magnetic Resonance in Medicine

Received: May 30, 2021 | Accepted: November 23, 2021

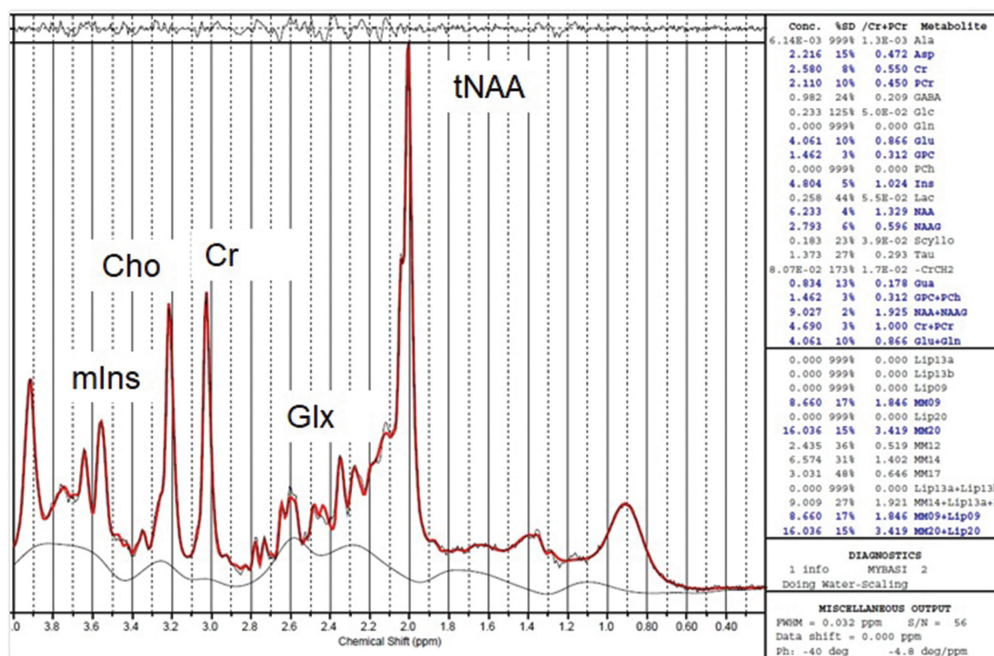


Fig. 1 A representative LCModel (Stephen Provencher, Oakville, Canada) output of *in vivo* ^1H -MR spectra for the centrum semiovale (8 mL) from a healthy volunteer. 3-T PRESS, TE/TR = 30/3000 ms; excitations = 128. Thin black lines are the original spectra; bold red lines represent fitted lines produced by the LCModel.⁷⁸ Cho, glycerophosphocholine (including choline-containing compounds) and phosphocholine; Cr, creatine and phosphocreatine; Glx, glutamate and glutamine; mIns, myo-inositol; PRESS, point-resolved spectroscopy; tNAA, N-acetylaspartylglutamate.

and methods may be applicable to MRS data of other anatomical regions, as well as those of other nuclei and MR spectroscopic imaging (MRSI).

MRS with a Clinical MR Scanner

Metabolites observed in human brain ^1H -MRS

Major metabolites

With *in vivo* ^1H -MRS of the brain, there are more than 30 observable metabolites, each with a variety of chemical shift value combinations.² The heights of each peak are proportional to the number of protons but decrease with longitudinal relaxation time (T_1), transverse relaxation time (T_2), and J-coupling inherent to each peak, with the degree of the decrease depending on the MRS sequence and its parameters, including TE and TR. However, if the TR is long enough, the peak is not affected by the T_1 (see 2.2.3 and 2.4 for more details). Furthermore, for *in vivo* human measurements, line broadening due to magnetic field inhomogeneity can cause peaks to overlap those of other metabolites or the metabolite peaks with low concentrations to be embedded in noise, meaning that about 5 or 6 metabolites can be clearly observed in a clinical MR scanner (Fig. 1). The typical brain metabolites observed by MRS with a 1.5-T or 3-T clinical MR scanner are NAA and N-acetylaspartylglutamate (tNAA); glycerophosphocholine (including choline-containing compounds) and phosphocholine (collectively referred to

here as Cho); creatine and phosphocreatine (collectively referred to here as Cr); glutamate (Glu) and glutamine (Gln) (collectively referred to here as Glx); Lac; and myo-inositol (mIns). The functions of these metabolites are shown in Table 1.^{2–25}

Other metabolites

Metabolites other than those mentioned above include taurine, ethanolamine, gamma aminobutyric acid (GABA), and glutathione (GSH), but these are usually at low concentrations (≤ 2.0 mM).^{2,26} In healthy individuals, their concentrations are not easy to measure accurately because their metabolite peaks overlap those of metabolites with higher concentrations such as Glu and Gln, but in specific pathological conditions, these metabolites may be identified by an increase in their concentration.²⁷ In addition, GABA and GSH can be measured using the J-difference editing method (e.g., MEGA-PRESS) with scanners over 2.0 T.^{28–32}

MR spectral quality in clinical ^1H MRS

The spectrum needs to have a good SNR. Improving SNR requires adjustment of the uniformity of the magnetic field, which affects the linewidth of the spectrum, and adjustment of sequence parameters such as TE and TR, voxel size, and the number of signal averages. The spectral quality may also be improved by correcting spectral distortion due to the eddy current effect.

Table 1 Brain metabolites typically detected by MRS with a 1.5- or 3-T clinical MR scanner

Metabolites	Comments
tNAA	NAA is produced in neuronal mitochondria and converted to N-acetylaspartylglutamate or transported to oligodendrocytes as a source of acetyl groups for myelin lipid synthesis. NAA is thought to correlate with the density of normal neurons, and a tNAA peak reduction is observed in many neurological disorders. The main peak from the acetyl group (CH ₃ CO-) is at 2.01 ppm. ^{2,7}
Cr	Cr acts as a “battery” for replenishing ATP levels. In adults, its concentration usually remains relatively stable during aging, as well as in a variety of diseases. Hence, it is sometimes used as the denominator of other metabolite ratios. The main peak from the methyl protons of both creatine and phosphocreatine is at 3.03 ppm. ^{2,6-9}
Cho	Cho is involved in various functions in the body, but the primary contributors to the Cho signal detected with ¹ H in normal tissue are PCho and GPC, and signal changes are generally associated with alterations in membrane and composition and are thought to often correlate with the destruction or enhancement of cell membrane metabolism. The main peak from the methyl protons of several choline-containing metabolites is at 3.2 ppm. ^{2,7,10,11}
Glx	Glu is an excitatory neurotransmitter, and Gln is involved in glutamate detoxification, osmolyte synthesis, and ammonia detoxification. At 1.5-T, there is substantial overlap between the Glu and Gln peaks, and it is difficult to separate these peaks with high reliability. The peaks are at about 2.1 to 2.6 ppm. ^{2,7,12,13}
mIns	mIns is an intracellular osmolyte found in astrocytes and a lipid metabolism precursor for membrane synthesis. Elevated mIns is considered to reflect an increased population of glial cells. It also plays roles in cellular nutrition and forms complexes, such as those with inositol-1-phosphate and phosphatidylinositol. At a short TE (~30 ms), its main peak is at 3.55 ppm and may contain a glycine peak. ^{2,7,14-18}
Lac	Lac is a metabolite produced by anaerobic glycolysis that is considered to be an indicator of the degree of energy metabolism disorder. Lac peaks in the brain have been observed during diseases such as mitochondrial disorders and are interpreted as an increase in anaerobic metabolism. In the newborn period, Lac peaks are often observed, even under healthy conditions, and it is considered to an important energy source for the brain. The peaks are at about 1.33 ppm, and lipid and/or macromolecule peaks may overlap them at a short TE (~30 ms). ^{2,7,19-25}

ATP, adenosine triphosphate; Cho, glycerophosphocholine (including choline-containing compounds) and phosphocholine; Cr, creatine and phosphocreatine; Gln, glutamine; Glu, glutamate; Glx, glutamate and glutamine; GPC, glycerophosphorylcholine; Lac, lactate; mIns, myo-Inositol; MRS, MR spectroscopy; NAA, NAA, n-acetyl aspartate; PCho, phosphorylcholine; tNAA, N-acetylaspartate and N-acetylaspartylglutamate.

SNR

The SNR is defined as the ratio of the largest metabolite peak height to twice the root-mean-square standard deviation of the noise in areas with no peaks and/or artifacts of the spectrum in the frequency domain (Fig. 2).^{33,34} However, it is sometimes defined as the ratio of the largest metabolite peak height to the root-mean-square standard deviation or the free induction decay (FID) signal amplitude at t = 0 divided by the noise at the end of the FID in the time domain.³⁵

Linewidth

The full-width at half-maximum (FWHM) of the spectral height is usually used as the definition of linewidth (Fig. 3). The FWHM of a metabolite or water peak is determined by its T₂ and the local inhomogeneity of the magnetic field (ΔB₀).^{36,37} Furthermore, if the multiplication of any line as a window function is applied to the FID data before the Fourier transform, the related value will also be included in the FWHM of the spectral data.

$$FWHM = \frac{1}{\pi T_2} + \gamma \Delta B_0 + (WinFunc) \quad [1]$$

Here, γ is the gyromagnetic ratio and WinFunc is related to the multiplied window function value. The T₂ of the major brain metabolites (tNAA, tCr, tCho, mIns, Glx, and Lac) at 3-T is reported to be 134–318 ms,³⁸⁻⁴⁰ which means that

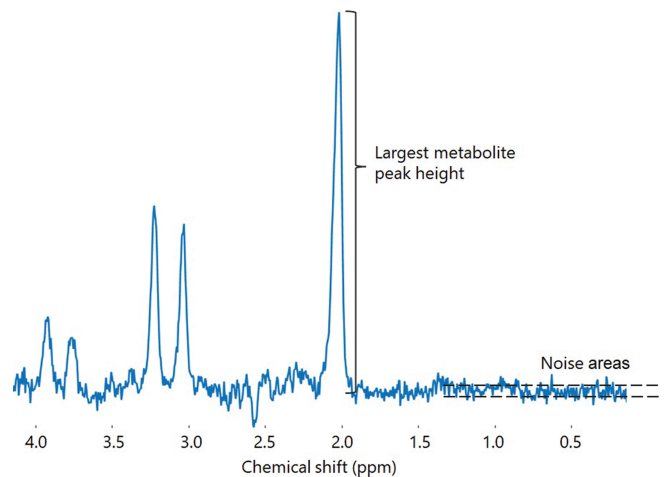


Fig. 2 Definition of the signal-to-noise ratio in the frequency domain.

$\frac{1}{\pi T_2}$ is calculated to be 1.0–2.4 Hz. To achieve local homogeneity, shimming is performed using a vendor-provided shim tool. Shimming methods include 3D shim, which is based on spherical harmonic analysis,⁴¹ and fast

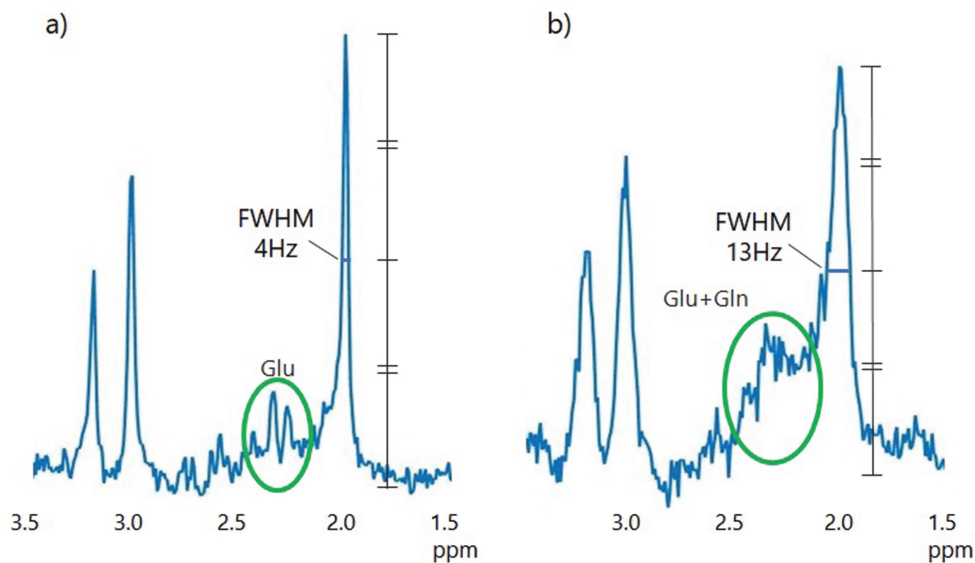


Fig. 3 Two representative spectra from *in vivo* human brain MRS. Although the peak of Glu is clearly observed in **a**), it seems difficult to separate the broad peaks into Glu and Gln in **b**). FWHM, full-width at half-maximum; Gln, glutamine; Glu, glutamate; MRS, MR spectroscopy.

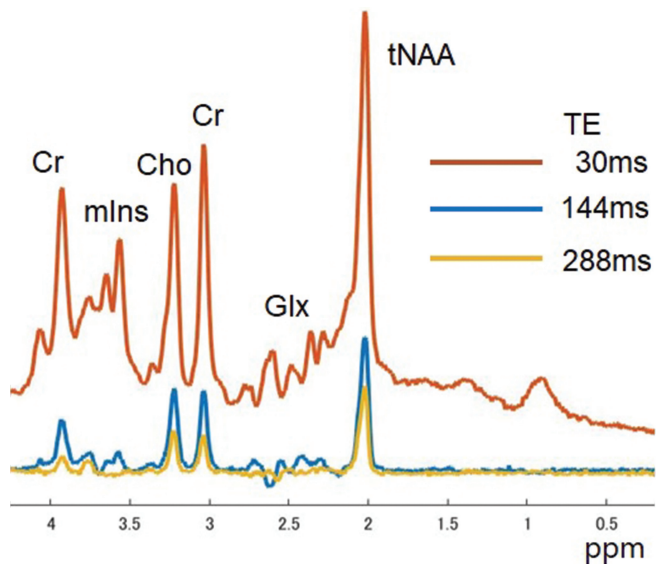


Fig. 4 Representative *in vivo* human brain ^1H -MR spectra with different TEs (30, 144, and 288 ms). Volume, 8 mL; TR, 3000 ms; number of signal averages, 128. Cho, glycerophosphocholine (including choline-containing compounds) and phosphocholine; Cr, creatine and phosphocreatine; Glx, glutamate and glutamine; mIns, myo-inositol; tNAA, N-acetylaspartylglutamate.

automatic shimming technique by mapping along projections (FASTMAP) shimming, which is based on measuring B_0 field plots along projections.⁴²

Voxel size, TE and TR, and number of signal averages

Voxel size: This parameter is also known as volume of interest (VOI). The SNR is said to be proportional to the

VOI³⁵ but the VOI is preferably 8 mL or less in *in vivo* brain MRS.

TE: A short TE (< 35 ms) avoids a signal decrease due to T_2 decay and signal phase modulation due to J-coupling and detects numerous metabolites (Fig. 4). However, macromolecules and/or lipids with a short T_2 and J-couplings are also detected as broad peaks (Fig. 4),^{43–45} and these broad peaks may interfere with the quantification of metabolite peaks. At a TE of 144 ms, the lactate peak (1.33 ppm) is inverted owing to the phase modulation by J-coupling (Fig. 5), and in addition, the macromolecules and lipid peaks are relaxed and phase-modulated, resulting in a significant decrease in peak height. Therefore, a TE of 144 ms (or 135 ms) is mainly used for Lac peak evaluation.⁴⁶ A longer TE is used to observe the metabolite peaks of a relatively longer T_2 .^{47–49} Moreover, for a metabolite with J-couplings between multiple ^1H s, the peak is decreased owing to the phase modulations with a longer TE time, as shown in Fig. 5.^{50,51} Therefore, a short TE is required to observe mIns, Glu, and/or Gln, and a TE setting of 144 ms or longer may be used to exclude other metabolites for the evaluation of tNAA, Cr, Cho, and/or Lac (Fig. 4).

TR: As for TR, it should be set to 2000 ms or more to avoid signal loss due to insufficient longitudinal relaxation with a too short TR (see Metabolite quantification for more details).

Number of signal averages: This parameter is also known as the number of excitations (NEX) in MRS. Because the SNR is said to be proportional to the square root of the number of signal averages, if the resulting spectrum does not have a sufficient SNR, an increase in the number of signal averages may give a better result.

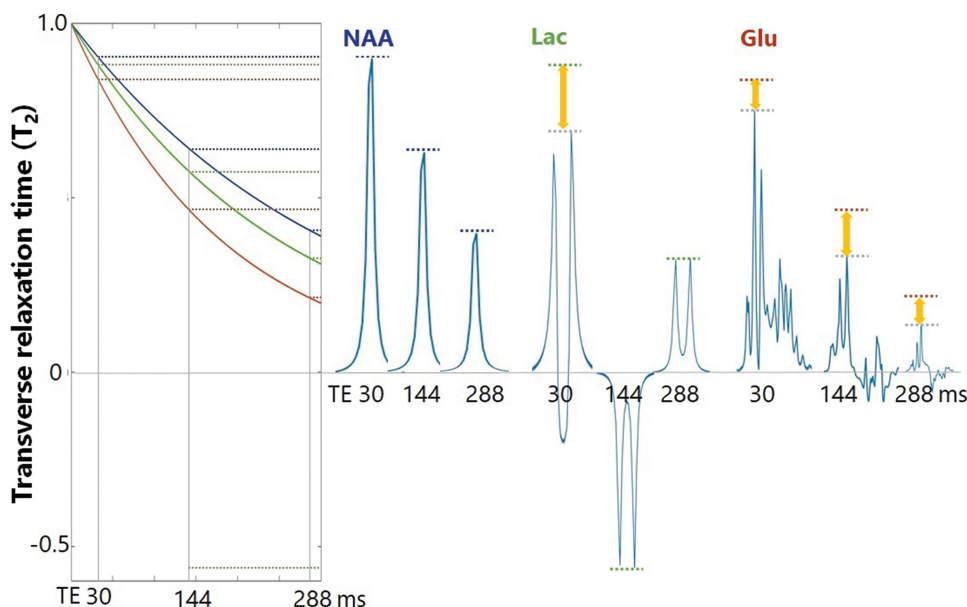


Fig. 5 T_2 decay curves vs. TE, and simulated spectra of NAA (2.0 ppm, blue), Lac (1.3 ppm, green), and Glu (1.9–2.4 ppm, red) at TE of 30, 144, and 288 ms. As the T_2 for NAA, Lac, and Glu, values of 305, 256 and 185 ms were used, respectively.^{39,40} Because there is no J-coupling in the NAA peak at 2.0 ppm, the peak decrease with an increasing TE is due only to T_2 . However, the J-coupling phase modulation is seen at the Lac and Glu peaks, and the peaks are further decreased by the phase modulation at a certain TE value (yellow arrows). Because two Lac peaks are in phase every 144 ms, the peak decreases at 144 and 288 ms are due only to T_2 . A set of spectra was simulated with FID-A.¹⁰⁴ FID, free induction decay; Glu, glutamate; Lac, lactate; NAA, n-acetyl aspartate

Eddy current effect correction

Eddy currents induced by rapid gradient switching generate short-time B_0 field fluctuations.^{35,43} If this fluctuation remains during the acquisition window, the FID data are affected by the fluctuation, which leads to MRS signal distortion (Fig. 6). Correction is performed by using a water-unsuppressed signal with an identical VOI, gradient strengths, and timings to the water-suppressed data. The same eddy current effects as the water-unsuppressed data are also included in the phases of the water-suppressed data. By subtracting this phase function from both the water-suppressed and water-unsuppressed FID signals, the spectra can be free from the eddy current effects (Fig. 6).

MRS data acquisition methods

MRS data collection methods include single-voxel MRS^{17,18,43,52–54} and MRSI, which is also called chemical shift imaging (CSI).^{17,18,55–61} Furthermore, VOI localization methods include localization by sequences such as point-resolved spectroscopy (PRESS)²⁸ and stimulated echo (STEAM),⁶² which generate a cube, rectangular, or parallelepiped voxel, and localization by a surface coil with a sequence such as depth-resolved sequence (DRESS),²⁸ which is often used when the target organ or tissue is in a region of the body other than the head and when the target nucleus is a non-proton nucleus, such as ^{13}C or ^{31}P .^{12,28,63–67}

Water signal suppression and outer volume suppression pulse

Prior to the execution of the localization sequence, water signal suppression and outer volume suppression (OVS) are

usually performed, as shown in Fig. 7. Water has a concentration of 10000 times or more than that of metabolites and, in the spectrum, distortion due to water peaks may make it difficult to quantify the metabolite peaks.⁶⁸ Therefore, a chemical shift selective (CHESS) pulse is used for the water signal suppression.^{17,18,69,70} The CHESS sequence comprises a frequency-selective RF pulse followed by a spoiler gradient. In a clinical MR scanner, three repetitions of CHESS pulses are used to enhance the water suppression effect; because the repetition of CHESS pulses generates unwanted echoes, the direction of the spoiler gradient is switched for each CHESS pulse (Fig. 7a1) or its intensity is gradually increased (Fig. 7a2).⁷⁰ When spectra of an identical VOI with a water-unsuppressed signal are also acquired to correct eddy current-induced phase shifts and quantify metabolite concentrations (see Eddy current effect correction and Metabolite quantification for more details), the CHESS RF pulse is specifically turned off and the spoiler gradient is used as is.^{43,71} OVS is a method for spatially saturating and reducing the signal outside the VOI.^{17,18,68,72–74} The strength of the slice gradient for the saturation pulse should be higher in order to minimize the chemical shift displacements of metabolites.^{17,18}

Single-voxel MRS

STEAM: The STEAM sequence⁶² is installed by default on MRI devices capable of MRS. The STEAM sequence uses three 90° pulses for localization and generates four to five echoes; the echo generated after the third 90° pulse is called the stimulated echo and is used in MRS as the desired signal (Fig. 7c1).^{18,41,62,75,76} Spoiler gradients destroy the echoes and FIDs outside the VOI. The interval between the second and third pulses is called the mixing time (TM). During the

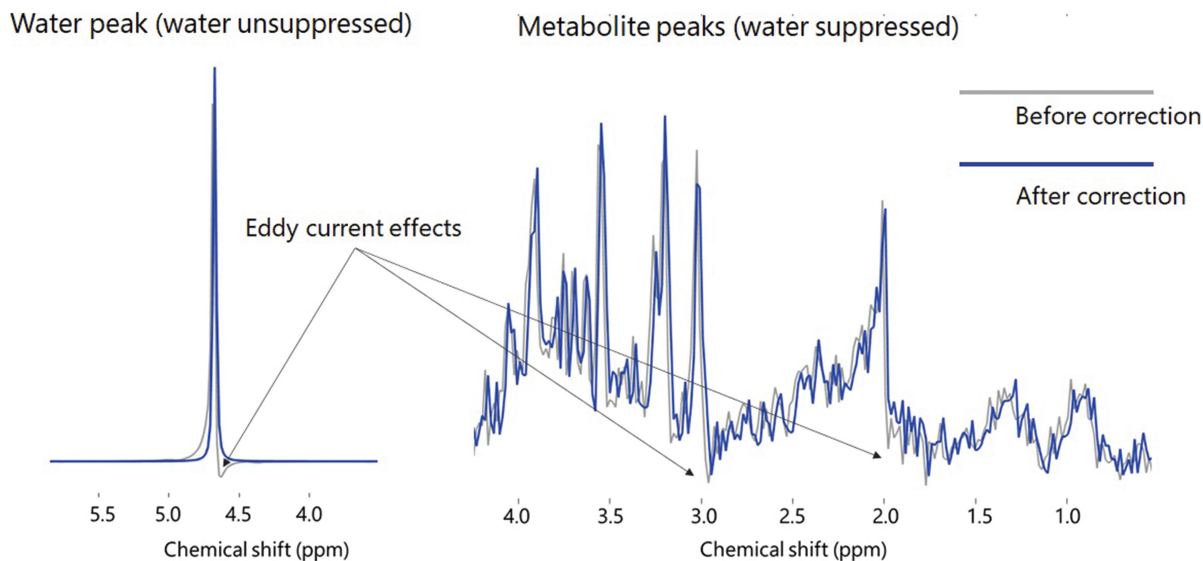


Fig. 6 Eddy current correction of *in vivo* human brain ^1H -MR spectra (PRESS, TE/TR = 30/5000 ms). Water-unsuppressed (left) and water-suppressed (right) spectra with eddy current artifacts (gray line) and after eddy current correction (blue line). PRESS, point-resolved spectroscopy.

TM period, the magnetization is at the longitudinal (z-) axis, has no transverse components, and does not experience T_2 decay. Therefore, the effective TE is the sum of the times between the first and second pulses (TE/2), and the third pulse and the signal acquisition (TE/2). The maximum signal intensity of the stimulated echo can be calculated as follows:

$$S \propto \frac{M_0}{2} \cdot \sin \alpha_1 \cdot \sin \alpha_2 \cdot \sin \alpha_3 \cdot \exp\left(\frac{-TE}{T_2}\right) \cdot \exp\left(\frac{-TM}{T_1}\right), \quad [2]$$

where M_0 is the equilibrium magnetization along the z-axis and α_i is the i th pulse angle. If each pulse is a perfect 90° , and TE and TM are both short enough compared with the T_1 and T_2 , the maximum possible signal is 50% of the M_0 .⁷⁶

PRESS: The PRESS sequence²⁸ is also installed by default on MRI devices capable of MRS. The PRESS sequence comprises mainly three slice-selective pulses (90° – 180° – 180°), each of which has a field gradient for localization, and a single voxel is finally excited. Spoiler gradients on both sides of the field gradient destroy the echoes and FIDs outside the VOI mainly generated by imperfect RF pulses^{18,28,41} (Fig. 7c2).

PRESS is more widely used because its SNR is twice of that of STEAM.^{18,76} However, the advantages of STEAM over PRESS are that (i) TE can be shortened in STEAM owing to the difference in the echo generation mechanism described above, and (ii) by using only 90° pulses, it has a sharper slice profile, a wider pulse bandwidth, smaller chemical shift displacements of metabolites, and a smaller specific absorption rate.^{18,41,77}

Metabolite quantification

There are several software packages for *in vivo* MRS data analysis, including LCModel, jMRUI, and Tarquin, all three of which are free to use.^{78–83} Here, we will consider LCModel and describe the output metabolite values. LCModel runs on Unix or Linux and quantitatively analyzes peaks of *in vivo* brain metabolites, muscle, or liver from the MRS data collected.^{34,79} LCModel uses linear analysis to separate a spectrum into peaks of individual metabolites by comparison with a set of model spectra, called a basis set (see the last paragraph of this section for more details). When FID data are input into the LCModel, preprocessing such as fast Fourier transform and phase correction^{43,54,84,85} is automatically performed, and the MR spectrum and various items are output, including the quantitative values of each metabolite, Conc., %SD, /Cr+PCr, and Metabolite (Fig. 1). The Conc. values of each metabolite are calculated using the following equation:

$$\text{Conc.} = \frac{\frac{\text{Metabolite peak area}}{\text{Metabolite proton numbers}}}{\frac{\text{Water peak area}}{\text{Water proton numbers}}} \times \text{Water concentration}, \quad [3]$$

where the metabolite peak area is that of the spectrum of the water-suppressed signal and the water peak area is that of the spectrum of the water-unsuppressed signal obtained from the identical VOI. The calculation process for Conc. does not consider the relaxation of the water and metabolite peaks. However, by default, only the water peak area is multiplied by 0.7, which takes into

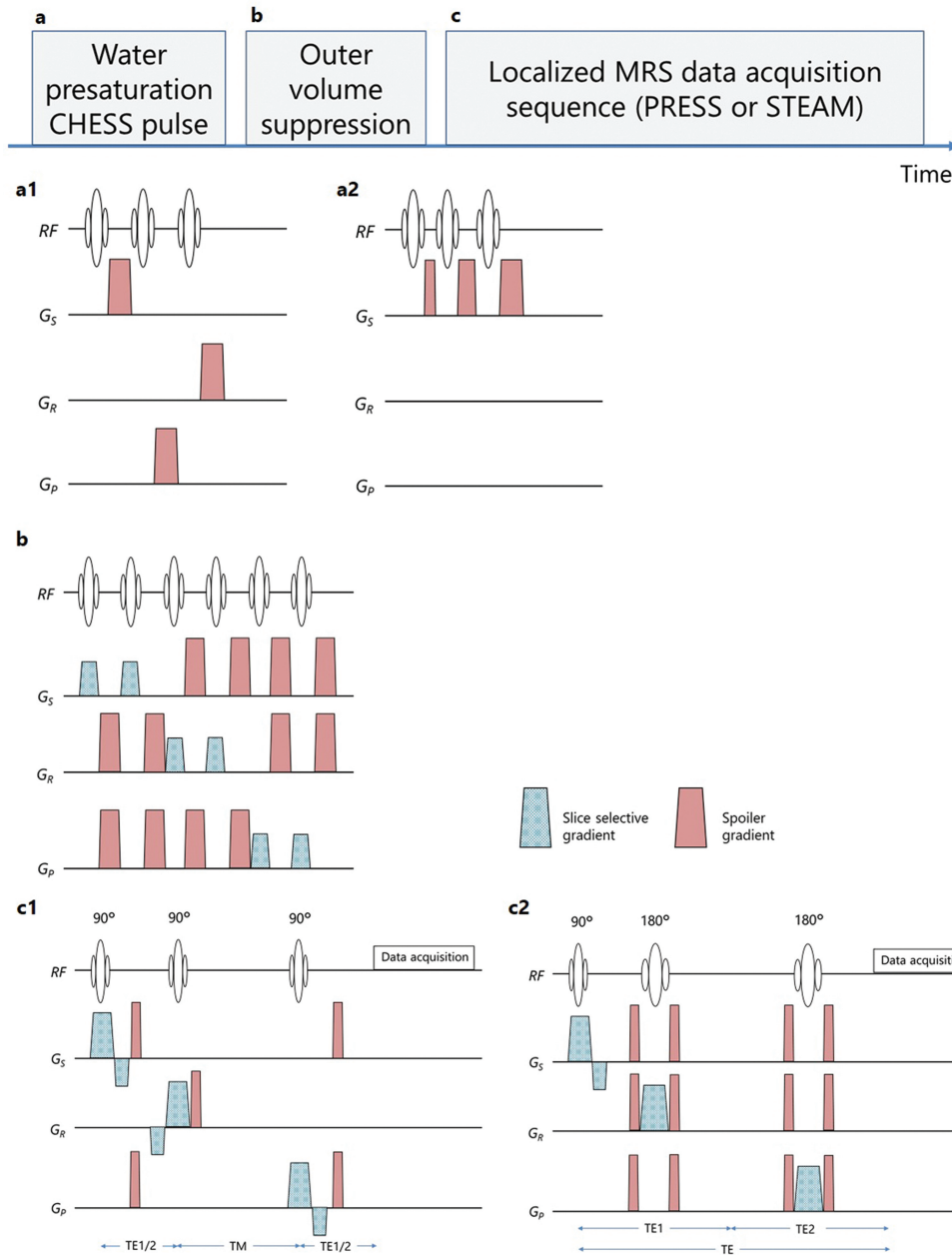


Fig. 7 An example of a single-voxel MRS scheme (not to scale). **a)** CHES pulse for water suppression. **b)** Outer volume suppression pulse. **c1)** STEAM sequence. TM = mixing time. **c2)** PRESS sequence. $TE1$ = first PRESS echo time; $TE2$ = second PRESS echo time.

account the reduction in the water peak by T_2 at $TE = 30$ ms.³⁴ The correction of the peak relaxation by T_1 and T_2 for water and metabolites will be discussed later. Water concentration describes the water concentration in the VOI. The default value is 35.88 M, which is that of adult white matter.³⁴ In addition, a concentration of 43.30 M is listed in the LCModel manual as that of adult gray matter.³⁴ However, the VOI region may contain a mixture of gray matter, white matter, and CSF,^{86,87} and the ratio of these components must be measured to more

accurately determine the water concentration. Moreover, water concentrations vary with age^{8,47,88,89} and may be altered in diseases such as edema and some tumors.⁹⁰⁻⁹² Therefore, it should be noted that serious errors in the results can occur if metabolite Conc. values are obtained using the same water concentration for different age groups, such as children and adults, or for healthy and disease groups.

Depending on the TE and TR settings, the water and metabolite peaks will decrease with their respective T_1 and

T_2 values as follows:

$$M_{xy} = M_0 \left\{ 1 - \exp\left(-\frac{TR}{T_1}\right) \right\} \cdot \exp\left(-\frac{TE}{T_2}\right), \quad [4]$$

where M_{xy} is the magnetization on the xy-transverse plane and M_0 is the equilibrium magnetization along the Z-axis. The first exponential equation is the M_0 recovery rate according to T_1 at $t = TR$, and the $M_0 \left\{ 1 - \exp\left(-\frac{TR}{T_1}\right) \right\}$ is equal to the M_{xy} magnetization just after being inverted to the xy-transverse plane by the 90° excitation pulse. The second exponential equation is the signal decay due to T_2 relaxation after excitation. Therefore, adding to Equation [3] a consideration of the decrease in metabolite and water peaks due to T_1 and T_2 , we get the following equation:

$$\frac{\frac{\text{Metabolite peak area}}{\text{Metabolite proton numbers}}}{\frac{\text{Water peak area}}{\text{Water proton numbers}}} \times \text{Water conc.} \times \frac{\left[1 - \exp\left(-\frac{TR}{\text{Water}T_1}\right) \right] \exp\left(-\frac{TE}{\text{Water}T_2}\right)}{\left[1 - \exp\left(-\frac{TR}{\text{Met}T_1}\right) \right] \exp\left(-\frac{TE}{\text{Met}T_2}\right)}, \quad [5]$$

Equations [4] and [5] show that the combination of a longer TR and shorter TE results in a smaller decrease in magnetization. At 1.5- and 3-T, the T_1 of adult brain metabolites is up to about 1.6 s,^{8,38,93–96} and if the TR is set to 5 s or more, that is, $\left\{ 1 - \exp\left(-\frac{TR}{T_1}\right) \right\} \approx 1$, it is not necessary to consider the correction of magnetization reduction by the T_1 . On the other hand, children have a higher brain water concentration and longer T_1 and T_2 compared with adults,^{8,47,89} and even adults may have a higher water concentration in pathological tissues such as tumors⁹¹ and may therefore need a longer TR setting to ignore the T_1 effect. To avoid the decrease in magnetization due to T_2 (and J-couplings, if present), a shorter TE is useful,^{8,38,43,47,49,89,97–102} but this needs to take into account the contribution of the macromolecule peaks (see Voxel size, TE and TR, and number of signal averages for more details). To determine the metabolite concentrations, it may also be necessary to consider the chemical shift displacements of metabolite peaks with different frequencies from the excitation frequency, which is usually set to the water resonance.^{18,103}

The value of %SD is equal to the Cramér–Rao lower bound and is used as an index of the uncertainty in the metabolite concentration estimates.³⁴ The /Cr+PCr for each metabolite represents the value of its metabolite value displayed in Conc. divided by that of Cr+PCr displayed in Conc.³⁴ The /Cr+PCr value (i.e., metabolite to Cr+PCr ratio) can be obtained without a water-unsuppressed spectrum and is a simpler method than that for determining the metabolite concentration.

The basis set must be a set of model spectra with the same pulse sequence, TE, and static field strength as the MRS data to be analyzed. Several basic sets are available for common measurement parameters, including TE 30 ms and 144 ms for 1.5-T and 3-T PRESS and STEAM sequences. If there is no basis set that matches the magnetic field strength, pulse sequence, and/or TE value of the MRS data to be analyzed, a basis set can be made from MRS data of the water solution phantom of metabolites³⁴ or by using simulation software such as FID-A.¹⁰⁴ In addition, to analyze the peaks of metabolites or drugs that are not included in the model spectrum, a basis set that incorporates those model peaks can be created.

Clinical utility of ^1H -MRS

Even in the 2010s, the clinical dissemination of ^1H -MRS as a routine diagnostic tool was very slow, and the availability of ^1H -MRS was generally limited to specialized institutions or hospitals with specialists in ^1H -MRS technology. The reasons for the limited clinical use of ^1H -MRS include its technical feasibility, lack of methodological standardization, and difficulties in interpretation. Some MR communities have published several excellent reviews to help establish a methodological and clinical consensus in the 2010s^{105,106} because the increased availability of 3-T MRI instruments was considered to be an excellent opportunity to promote clinical MRS. Our MRS community in the Japan Society of Magnetic Resonance in Medicine (JSMRM) published a consensus guideline in Japanese on the clinical utility of ^1H -MRS in 2013 (http://fa.kyorin.co.jp/jsmrm/haifuyo_new_MRS_guideline2013.pdf), which can be downloaded from the website of the society. Here, we have attempted to update this consensus guideline to include recent progress related to the technology and its generally accepted findings.

Physiological changes in metabolites with development and age observed with ^1H -MRS

The signals of major metabolites observed with ^1H -MRS are affected by brain development and aging, and their concentrations also differ among anatomical cerebral regions. The intensities of Cho and NAA signals are generally higher in white matter than in gray matter, whereas those of Cr, mIns, and Glx are higher in gray matter than in white matter.^{107,108} Furthermore, the intensities of Cr and Cho signals are usually highest in the cerebellum.¹⁰⁸

Many studies have shown that NAA and Cr signals are increased in childhood and that Cho and mIns signals decrease rapidly within the first year of life as development progresses, with a gradual decline until about 20 years of age.¹⁰⁷

In a systematic review of the brain metabolite changes measured by ^1H -MRS during healthy aging,^{109,110} most data were derived from the frontal region and indicated no change in older individuals in 18 studies. However, a meta-analysis

showed a decrease in frontal NAA and increases in parietal Cho and Cr. This review suggested that NAA may decrease, and Cho and Cr increase with age, and more data are therefore needed from older individuals to better characterize the effect of age. Accordingly, metabolite ratios in older people should be interpreted with caution.

Clinical utility in the diagnosis of brain tumors and tumor-like disorders

The clinical utility of ^1H -MRS can largely be classified into five categories: 1) grading of gliomas, 2) evaluation of therapeutic effects, including differentiation between recurrence and radiation necrosis, 3) differentiation between gliomas and brain metastasis, 4) differentiation between cystic tumors and brain abscess, and 5) prediction of isocitrate dehydrogenase (IDH) mutant gliomas using the detection of 2-hydroxyglutarate (2-HG).

For glioma grading, several studies have reported that automated algorithms can classify high- and low-grade gliomas with sensitivity and specificity exceeding 90%. However, the accuracy of the differentiation between grade III and IV is lower.¹¹¹ Regarding the evaluation of therapeutic effects, increases in Cho or in the signal ratios of Cho/Cr and Cho/NAA were related to tumor recurrence or a low therapeutic effect, whereas low levels of Lac and Lip were found in good responders to tamoxifen.¹¹² The accuracy of the differentiation between gliomas and metastasis was 60%–80% and lower than that of the grading of glioma (about 90%).^{113,114} The ability to differentiate between gliomas and metastasis was suggested to be related to a greater increase in lipids in metastasis than in gliomas. Cystic tumors and abscess were successfully differentiated using the signal derived from succinate, acetate, alanine, and glycine, with 96% sensitivity and 100% specificity.¹¹⁵

IDH mutant gliomas have recently received more attention due to their better prognosis than IDH wild-type gliomas. IDH overproduces 2-HG, which is a suitable biomarker of IDH mutant glioma. 2-HG has five protons with a complicated J-coupling interaction and shows complicated multiplet signals at about 1.9 ppm, 2.3 ppm, and 4.0 ppm. These signals usually overlap the major peaks of NAA, Glx, and Cr, and accurate detection of 2-HG by ^1H -MRS is therefore difficult and is still undergoing refinement. Thus far, several ^1H -MRS methods have been proposed, such as a short TE⁶² or long TE¹¹⁶ conventional ^1H -MRS sequence using prior-knowledge spectral analysis software (e.g., LCModel), the difference editing technique,¹¹⁷ and the 2D method.¹¹⁸ Most of the studies have been conducted using a conventional sequence with specific analysis software and showed higher sensitivity than specificity, with ranges of 77%–100% for sensitivity and 72%–100% for specificity.^{62,117–119} Although a few studies have been performed with the difference editing technique, a recent prospective study using spectral editing MRS with jMRUI software showed a sensitivity of 80% and specificity of 81%.¹²⁰ Preoperative edited MRS also

appears to be able to help identify IDH mutant gliomas with high specificity, but the accuracy requires improvement.

Clinical utility of ^1H -MRS in neurodegenerative diseases

Neurodegenerative diseases, which include Alzheimer disease, Parkinson disease, Huntington disease, amyotrophic lateral sclerosis, and multiple system atrophy, have been studied using clinical ^1H -MRS. Most of the studies concern Alzheimer disease and other types of dementia. In Alzheimer disease, the major findings were a decrease in NAA and Glu and increase in mIns in the affected regions.^{121–123} The decrease in NAA in the affected brain region is consistent with that of other neurodegenerative diseases, but the tendency was not disease-specific. Several studies have monitored the treatment response in Alzheimer disease. A transient increase in NAA concentration was associated with a short-term functional response during donepezil treatment in Alzheimer disease, indicating that NAA also reflects functional integrity and recovery.^{124,125} It is considered that the utility of ^1H -MRS will be in patient management rather than in disease diagnosis.

Clinical utility of ^1H -MRS in pediatric brain disorders

^1H -MRS can be used to detect characteristic metabolic changes, especially in metabolic or degenerative pediatric diseases, such as lysosomal storage disease, peroxisome disease, and mitochondria disease. ^1H -MRS is sometimes more useful than MRI-mediated morphological diagnosis in certain metabolic or degenerative diseases,¹⁰⁵ and its utility can be classified into the following four categories. Although these categories comprise rare diseases, ^1H -MRS plays significant roles in their clinical diagnosis.

Deficiency in Cr signals

Three metabolite diseases have thus far been reported in this category. Guanidinoacetate methyltransferase (GAMT) deficiency and creatine transporter (CRTR) deficiency show a loss of Cr signal and an increase in guanidinoacetate, which is a precursor of Cr, with signals appearing at about 3.7–3.9 ppm.^{126,127} Arginine:glycine amidinotransferase (AGAT) deficiency also shows a loss of Cr signal, with no increased signal from metabolites.¹²⁸

Increased NAA signal

Canavan disease and Salla disease are the two representative diseases in this category. Canavan disease causes decreased activity in aspartoacylase, which induces NAA accumulation. In addition, Cr and Cho are decreased and mIns is increased.¹²⁹ Salla disease is an abnormality in sialic acid metabolism that involves the accumulation of n-acetylneuraminic acid (NANA), whose signal is close to that of NAA, which complicates their differentiation. This disease may be recognized as an increase in NAA signal, especially at 1.5-T.¹³⁰ Furthermore, Pelizaeus-Merzbacher

disease is also known by an increase in NAA and Cr, and decrease in Cho.

Appearance of specific peaks that cannot usually be identified

a) Sjögren–Larsson syndrome: This disease is an abnormality in lipid metabolism involving a deficiency in fatty aldehyde dehydrogenase. The peaks derived from long-chain fatty alcohols are found at 0.9 and 1.3 ppm. A peak is observed at 0.9 ppm with a short TE sequence due to the short T_2 values of this metabolite.¹³¹

b) Succinate dehydrogenase deficiency: This disease is a type of mitochondrial encephalopathy. The peak of succinate is found at 2.4 ppm, in addition to the Lac peak.¹³²

c) Maple syrup urine disease: This disease is an abnormality in branched chain amino acid metabolism. The peaks of valine, leucine, and isoleucine are observed at 0.9–1.0 ppm, in addition to a decrease in NAA and an increase in Lac.¹³³

d) Galactosemia: This disease is caused by an abnormality in an enzyme related to galactose metabolism. The peaks of galactitol are found at 3.67 and 3.74 ppm.¹³⁴

e) Nonketotic hyperglycinemia: This disease is due to an abnormality in the glycine cleavage enzyme. A peak in glycine is observed at 3.55 ppm, which overlaps with that of mIns.¹³⁵ However, the T_2 value of glycine is much longer than that of mIns, which means that the peak at 3.55 ppm is usually observed in these patients with a long TE sequence. There are no abnormalities in NAA, Cr, and Cho with this disease.

f) Ribose-5-phosphate isomerase deficiency: This disease involves an abnormality in polyol metabolism. $^1\text{H-MRS}$ shows peaks of D-arabitol and ribitol at 3.6 and 3.8 ppm, respectively, which reflect the accumulation of polyols.¹³⁶

g) Sandhoff disease: This lysosomal disease is caused by a deficiency in hexosaminidases A and B. The peak of N-acetylhexosamine is found at 2.07 ppm, and $^1\text{H-MRS}$ also detects a decrease in NAA and increase in mIns.¹³⁷

h) GABA transaminase deficiency: Glu is metabolized to succinate from GABA through succinic semialdehyde. This pathway is called the GABA shunt. This disease causes an increase in GABA and $^1\text{H-MRS}$ can show the increase in GABA signal.²⁷

i) 3-hydroxy-3-methylglutaryl-CoA lyase (HMG-CoA) deficiency: HMG-CoA is transferred to acetyl-CoA and individuals with this deficiency show a peak at 2.42 ppm from 3-hydroxyisovalerate and 3-hydroxy-3-methylglutarate.¹³⁸ In addition, $^1\text{H-MRS}$ also identifies a decrease in NAA and increases in Cho and mIns.

Clinical studies of developmental disorders

Developmental disorders, including autism spectrum disorder, are an important target for clinical pediatric investigation and

many studies have reported pathophysiological changes in this disorder using $^1\text{H-MRS}$. However, the difference in metabolites between developmental disorder and normal development has not been characterized, and $^1\text{H-MRS}$ is not considered useful for the diagnosis of this disorder. On the other hand, oxytocin has recently been reported to be useful for improving autistic behavior, with its effect revealed in a randomized controlled trial using $^1\text{H-MRS}$ and functional MRI.¹³⁹ $^1\text{H-MRS}$ may be useful for evaluating the improvement in brain function with some medications.

Clinical utility of $^1\text{H-MRS}$ in psychological disorders

Schizophrenia

Of psychological disorders, schizophrenia is the most popular target for clinical $^1\text{H-MRS}$. The main findings of schizophrenia are decreased NAA or NAA/Cr in the frontal lobe, thalamus, hippocampus, and temporal lobe.^{140,141} On the other hand, there are no significant differences in Cr and Cho between schizophrenic and healthy individuals. However, these findings are not specific to schizophrenia alone, and the utility of $^1\text{H-MRS}$ in clinical diagnosis remains low.

Major depression

The number of published studies concerning major depression is lower than that for schizophrenia, and there is no difference in NAA between individuals with major depression and healthy people in most previous work. Some studies suggested a decrease in Cho/Cr in the basal ganglia and a decrease in Glx in the frontal lobe,^{142,143} and one study indicated a decrease in GABA in the posterior lobe with a 3-T MRI instrument.¹⁴⁴

Bipolar disorders and anxiety disorders

There are, thus far, no consistent findings of $^1\text{H-MRS}$ in bipolar disorder and anxious disorder. Several studies showed decreased NAA or NAA/Cr in the basal ganglia and hippocampus in bipolar disorder,¹⁴⁵ but others reported no change in NAA. In anxiety disorder, functional MRI suggested abnormalities in the orbitofrontal cortex, caudate nucleus, and thalamus, but there is no consensus on the changes in metabolites observed with $^1\text{H-MRS}$. The utility of $^1\text{H-MRS}$ in bipolar and anxiety disorders is limited to the clinical diagnosis and evaluation of therapeutic efficacy.

Utility of $^1\text{H-MRS}$ in demyelinating diseases (multiple sclerosis, clinically isolated syndrome, and neuromyelitis optica spectrum)

The utility of $^1\text{H-MRS}$ in the diagnosis of multiple sclerosis (MS) can be summarized as follows: 1) comprehension of the pathological changes in the plaques and normal-appearing white matter (NAWM); 2) evaluation of the therapeutic efficacy and monitoring of the clinical course; and 3) prediction of the transformation from clinically isolated syndrome (CIS). The typical findings of MS are increases in Cho, Lac,

Lip, mIns, and Glu and a decrease in NAA in the acute phase; in the chronic phase, the decrease in NAA and the increase in mIns continue, but the signals of Lac, Cho, and Lip gradually normalize.¹⁴⁶ The increase in Glu is limited in the acute phase and may be related to Glu-associated axonal injury and toxicity. In particular, a prominent increase in Glx has been found in tumefactive MS.¹⁴⁷ One study determined an increase in mIns only in MS plaques, and not in NAWM, and mIns may be used to differentiate between MS plaques and NAWM. Therapy responders showed an increase in NAA/Cr.¹⁴⁸ Several studies reported predictors of the transformation from CIS to MS, and useful predictors may be a significant decrease in NAA in NAWM in the early phase and an increase in mIns.^{149,150}

¹H-MRS studies in patients with neuromyelitis optica (NMO) spectrum disorder are still limited, but most of the studies found that the differentiating finding of NMO from MS is the lack of metabolite abnormalities in NAWM in patients with NMO, except for mIns.¹⁵¹

Acute ischemic disease

Multiple studies have evaluated acute ischemic lesions with ¹H-MRS, with decreased NAA and increased Lac consistent findings in acute ischemia,^{152,153} which are related to mitochondrial function and energy failure. One study reported an increase in Lac in the ischemic lesion before the appearance of a high signal in diffusion-weighted imaging.¹⁵⁴ However, no study has determined the level of metabolites on ¹H-MRS at which thrombolysis therapies should be applied, and there is no consensus on a suitable quantification method for application to acute ischemic diseases. To avoid time-consuming processes that delay clinical decision-making, further improvements in the measurement time and simplification of the procedure for accurate quantification are required to enable a multicenter prospective study to determine the threshold for the application of thrombolysis in patients with acute ischemic attacks.

Nuclei other than protons possibly useful in clinical MRS

Besides protons, all nuclei with a magnetic moment can theoretically be used for nuclear magnetic resonance (NMR).¹⁵⁵ Since the NMR frequency of each nucleus in a static magnetic field is different, it is necessary to install a transmission and reception system in the MR system and to prepare coils that support the frequency. *In vivo* MRS of nuclei other than protons has been performed for decades, but its application to *in vivo* humans has been enabled by the recent increase in static magnetic field strength and advances in fast and efficient sampling and reconstruction techniques.^{43,61,156,157} The nuclei other than protons that may be useful in clinical MRS in the coming years are ¹³C, ¹⁷O, ²³Na, and ³¹P. Their nuclear spin properties are

summarized in Table 2. Relative receptivity is obtained with the following equation:¹⁵⁸

$$R_A(X) = \left\{ \frac{\gamma(X)}{\gamma(A)} \right\}^3 \times \frac{I(X)\{I(X) + 1\}}{I(A)\{I(A) + 1\}} \times \frac{N_{abd}(X)}{N_{abd}(A)} \quad [6]$$

where $R_A(X)$ is the relative receptivity of nucleus X, A is a reference nucleus such as ¹H, γ is the gyromagnetic ratio, I is the spin quantum number, and N_{abd} is natural abundance.

¹³C: Its natural abundance is about 1%. Oral or intravenous administration of labeled [¹⁻¹³C] D-glucose and/or [²⁻¹³C] has been used to monitor the cerebral tricarboxylic acid (TCA) cycle, the Glu–Gln cycle, the metabolism from glucose to amino acids in the brain, the cerebral metabolic rate of oxygen consumption (CMRO₂), and the amount of glucose and glycogen in the liver.^{12,67,159–163} With the hyperpolarization (HP) technique, ¹³C-labeled substances increase their MRI signals at a rate of > 10000.^{18,164–166} [¹⁻¹³C]Pyruvate has been approved for use in clinical HP studies by the US Food and Drug Administration and has been used to monitor some metabolic pathways, such as glycolysis, the TCA cycle, and amino acid biosynthesis.¹⁶⁶ *In vivo* human studies have reported metabolic changes in patients with prostate cancer, brain tumor, or breast cancer.^{167–169} Other ¹³C HP probes used comprise endogenous biomolecules such as [²⁻¹³C]pyruvate for probing mitochondrial metabolism^{170–172} and ¹³C urea for imaging perfusion.¹⁷³

¹⁷O: ¹⁷O has a spin of 5/2, but the ¹⁷O₂–gas phase and ¹⁷O₂ dissolved in water have strong paramagnetism and hence are undetectable in ¹⁷O NMR. The ¹⁷O signal becomes detectable only when ¹⁷O is incorporated into water.¹⁶² ¹⁷O has been used to measure the CMRO₂ and as a contrast agent.^{162,174–182} There are two types of ¹⁷O-based NMR approaches. One approach involves the direct detection of ¹⁷O signal from H₂¹⁷O by intravenous injection of H₂¹⁷O or by inhalation of ¹⁷O₂ gas, which is converted to H₂¹⁷O via oxidative phosphorylation in the brain.^{162,174,178–181} The second approach is to indirectly detect ¹⁷O with ¹H-MRI. The protons in H₂¹⁷O have various Larmor frequencies due to scalar coupling with O-17.¹⁸³ The chemical exchange of water protons among H₂¹⁷O and H₂¹⁶O makes the T₂ of the water protons shorter. As a result, the T₂-weighted imaging signal intensity of the region including H₂¹⁷O is lower than that containing only H₂¹⁶O. Therefore, it is used to observe water flow by dynamic T₂-weighted ¹H-MRI.^{175–177,182,184–187}

²³Na: Its natural abundance is 100%. ²³Na has a spin of 3/2, which causes electrostatic field sensitivity and fast T₂* signal decay.^{41,188,189} ²³Na is endogenous to human tissue and can be imaged without external contrast. The concentration of sodium ions (Na⁺) is reported to be raised in solid tumors, and *in vivo* human ²³Na-MRI studies have been conducted in patients with brain tumor, breast tumors, prostate cancer, and serous ovarian cancer.^{190–196}

Table 2 Nuclear spin properties

Nucleus	Spin quantum number	Gyromagnetic ratio (g) (MHz/T)	Natural abundance (%)	Relative receptivity
¹ H	1/2	42.58	99.99	1.000
¹³ C	1/2	10.71	1.08	1.72 × 10 ⁻⁴
¹⁷ O	5/2	-5.77	0.04	1.16 × 10 ⁻⁵
²³ Na	3/2	11.26	100.00	9.25 × 10 ⁻²
³¹ P	1/2	17.24	100.00	6.64 × 10 ⁻²

³¹P: Its natural abundance is 100%. In ¹H-MRS, Cho, phosphocholine (PCho), and glycerophosphocholine are observed as total Cho, with ¹H from the methyl group (-CH₃) having almost the same chemical shift value (3.2 ppm).² However, ³¹P-MRS, PCho, and glycerophosphocholine have a phosphate group, and the chemical shift value of each ³¹P is different and individual quantification is possible.¹⁰ *In vivo* ³¹P-MRS provides information on energy metabolism, cell membrane, and pH by monitoring peaks, such as adenosine triphosphate and phosphocreatine, phosphomonoesterase and phosphodiesterase, and inorganic phosphate, respectively.^{10,11,17,18,41,197,198} Especially in cancer, Cho phospholipid metabolism, particularly PCho and tCho, are elevated and can be used in cancer diagnosis and staging by using ³¹P-MRS.^{10,11,17,18,199–201}

Acknowledgment

The authors of the “Consensus Guidelines for the Clinical Utility of proton MRS” published in 2013 (http://fa.kyorin.co.jp/jsmrm/haifuyo_new_MRS_guideline2013.pdf) were Drs. Masaharu Ida, Yasushi Kaji, Hirohiko Kimura, Mariko Toyooka, Toshinori Hirai, Hitoshi Kubo, Jyunnichi Takanashi, Takayuki Obata, Noriko Aida, Masafumi Harada, Kaori Furutani, and Satsuki Sumitani.

Funding

The authors thank Dr. Tsuyoshi Matsuda for his advice on the contents. MT is supported by the Japan Society for the Promotion of Science (JSPS) KAKENHI [Grant Numbers 15K09943 and 19K08213].

Conflicts of Interest

The authors have no conflicts of interest.

References

1. Tsai G, Coyle JT. N-acetylaspartate in neuropsychiatric disorders. *Prog Neurobiol* 1995; 46:531–540.
2. Govindaraju V, Young K, Maudsley AA. Proton NMR chemical shifts and coupling constants for brain metabolites. *NMR Biomed* 2000; 13:129–153.

3. Parsons MW, Li T, Barber PA, et al. Combined (1)H MR spectroscopy and diffusion-weighted MRI improves the prediction of stroke outcome. *Neurology* 2000; 55:498–505.
4. Caramanos Z, Narayanan S, Arnold DL. 1H-MRS quantification of tNA and tCr in patients with multiple sclerosis: a meta-analytic review. *Brain* 2005; 128:2483–2506.
5. Moffett JR, Ross B, Arun P, Madhavarao CN, Namboodiri AM. N-Acetylaspartate in the CNS: from neurodiagnostics to neurobiology. *Prog Neurobiol* 2007; 81:89–131.
6. Benarroch EE. N-acetylaspartate and N-acetylaspartylglutamate: neurobiology and clinical significance. *Neurology* 2008; 70:1353–1357.
7. Panigrahy A, Nelson MD, Blüml S. Magnetic resonance spectroscopy in pediatric neuroradiology: clinical and research applications. *Pediatr Radiol* 2010; 40:3–30.
8. Kreis R, Ernst T, Ross BD. Development of the human brain: in vivo quantification of metabolite and water content with proton magnetic resonance spectroscopy. *Magn Reson Med* 1993; 30:424–437.
9. Voet D, Voet JG, Pratt CW. *Fundamentals of Biochemistry: Life at the Molecular Level*, 5th ed. Hoboken:Wiley,2016.
10. Glunde K, Bhujwala ZM, Ronen SM. Choline metabolism in malignant transformation. *Nat Rev Cancer* 2011; 11:835–848.
11. Glunde K, Penet MF, Jiang L, Jacobs MA, Bhujwala ZM. Choline metabolism-based molecular diagnosis of cancer: an update. *Expert Rev Mol Diagn* 2015; 15:735–747.
12. Shen J, Petersen KF, Behar KL, et al. Determination of the rate of the glutamate/glutamine cycle in the human brain by in vivo ¹³C NMR. *Proc Natl Acad Sci U S A* 1999; 96:8235–8240.
13. Verkhratsky A, Butt A. *Glial Neurobiology: A textbook*. Chichester:John Wiley & Sons, 2007.
14. Heindel W, Kugel H, Roth B. Noninvasive detection of increased glycine content by proton MR spectroscopy in the brains of two infants with nonketotic hyperglycinemia. *AJNR Am J Neuroradiol* 1993; 14:629–635.
15. Strange K, Emma F, Paredes A, Morrison R. Osmoregulatory changes in myo-inositol content and Na⁺/myo-inositol cotransport in rat cortical astrocytes. *Glia* 1994; 12:35–43.
16. Howe FA, Barton SJ, Cudlip SA, et al. Metabolic profiles of human brain tumors using quantitative in vivo ¹H magnetic resonance spectroscopy. *Magn Reson Med* 2003; 49:223–232.
17. Barker PB, Bizzi A, Stefano ND, Gullapalli R, Lin DDM. *Clinical MR Spectroscopy: Techniques and Applications*. New York:Cambridge University Press, 2009.

18. Bottomley PA, Griffiths JR, Harris RK, et al. Handbook of magnetic resonance spectroscopy in vivo: MRS theory, practice and applications. Chichester: John Wiley & Sons, 2016.
19. Detre JA, Wang ZY, Bogdan AR, et al. Regional variation in brain lactate in Leigh syndrome by localized 1H magnetic resonance spectroscopy. *Ann Neurol* 1991; 29:218–221.
20. Mathews PM, Andermann F, Silver K, Karpati G, Arnold DL. Proton MR spectroscopic characterization of differences in regional brain metabolic abnormalities in mitochondrial encephalomyopathies. *Neurology* 1993; 43:2484–2490.
21. Barkovich AJ, Good WV, Koch TK, Berg BO. Mitochondrial disorders: analysis of their clinical and imaging characteristics. *AJNR Am J Neuroradiol* 1993; 14:1119–1137.
22. Leth H, Toft PB, Pryds O, Peitersen B, Lou HC, Henriksen O. Brain lactate in preterm and growth-retarded neonates. *Acta Paediatr* 1995; 84:495–499.
23. Rinholm JE, Hamilton NB, Kessaris N, Richardson WD, Bergersen LH, Attwell D. Regulation of oligodendrocyte development and myelination by glucose and lactate. *J Neurosci* 2011; 31:538–548.
24. Xu D, Bonifacio SL, Charlton NN, et al. MR spectroscopy of normative premature newborns. *J Magn Reson Imaging* 2011; 33:306–311.
25. Tomiyasu M, Aida N, Shibasaki J, et al. Normal lactate concentration range in the neonatal brain. *Magn Reson Imaging* 2016; 34:1269–1273.
26. Murali-Manohar S, Borbath T, Wright AM, Soher B, Mekle R, Henning A. T2 relaxation times of macromolecules and metabolites in the human brain at 9.4 T. *Magn Reson Med* 2020; 84:542–558.
27. Tsuji M, Aida N, Obata T, et al. A new case of GABA transaminase deficiency facilitated by proton MR spectroscopy. *J Inher Metab Dis* 2010; 33:85–90.
28. Bottomley PA. Spatial localization in NMR spectroscopy in vivo. *Ann N Y Acad Sci* 1987; 508:333–348.
29. Rothman DL, Petroff OA, Behar KL, Mattson RH. Localized 1H NMR measurements of gamma-aminobutyric acid in human brain in vivo. *Proc Natl Acad Sci U S A* 1993; 90:5662–5666.
30. Mescher M, Mekle H, Kirsch J, Garwood M, Gruetter R. Simultaneous in vivo spectral editing and water suppression. *NMR Biomed* 1998; 11:266–272.
31. Terpstra M, Henry PG, Gruetter R. Measurement of reduced glutathione (GSH) in human brain using LCModel analysis of difference-edited spectra. *Magn Reson Med* 2003; 50:19–23.
32. Puts NA, Edden RA. In vivo magnetic resonance spectroscopy of GABA: a methodological review. *Prog Nucl Magn Reson Spectrosc* 2012; 60:29–41.
33. Freeman R. Sensitivity. In: *A handbook of nuclear magnetic resonance*, 2nd ed. Harlow: Addison-Wesley Longman, 1997; 248–255.
34. Provencher S. LCModel¹ & LCMgui User's Manual. <http://s-provencher.com/pub/LCModel/manual/manual.pdf>. (Accessed: November 14, 2021)
35. Kreis R. Issues of spectral quality in clinical 1H-magnetic resonance spectroscopy and a gallery of artifacts. *NMR Biomed* 2004; 17:361–381.
36. Farrar T, Becker E. Basic concepts in NMR. In: *Pulse and fourier transform NMR*. New York: Academic Press, 1971; 1–17.
37. Li BS, Regal J, Gonen O. SNR versus resolution in 3D 1H MRS of the human brain at high magnetic fields. *Magn Reson Med* 2001; 46:1049–1053.
38. Mlynárik V, Gruber S, Moser E. Proton T (1) and T (2) relaxation times of human brain metabolites at 3 Tesla. *NMR Biomed* 2001; 14:325–331.
39. Madan A, Ganji SK, An Z, et al. Proton T2 measurement and quantification of lactate in brain tumors by MRS at 3 Tesla in vivo. *Magn Reson Med* 2015; 73:2094–2099.
40. Zhang Y, Shen J. Simultaneous quantification of glutamate and glutamine by J-modulated spectroscopy at 3 Tesla. *Magn Reson Med* 2016; 76:725–732.
41. Elster AD. *Questions and answers in MRI*. Toronto: Mosby, 1994.
42. Gruetter R. Automatic, localized in vivo adjustment of all first- and second-order shim coils. *Magn Reson Med* 1993; 29:804–811.
43. Near J, Harris AD, Juchem C, et al. Preprocessing, analysis and quantification in single-voxel magnetic resonance spectroscopy: experts' consensus recommendations. *NMR Biomed* 2021; 34:e4257.
44. Pfeuffer J, Tkáč I, Provencher SW, Gruetter R. Toward an in vivo neurochemical profile: quantification of 18 metabolites in short-echo-time (1)H NMR spectra of the rat brain. *J Magn Reson* 1999; 141:104–120.
45. de Graaf RA, Brown PB, McIntyre S, Nixon TW, Behar KL, Rothman DL. High magnetic field water and metabolite proton T1 and T2 relaxation in rat brain in vivo. *Magn Reson Med* 2006; 56:386–394.
46. Lunsing RJ, Strating K, de Koning TJ, Sijens PE. Diagnostic value of MRS-quantified brain tissue lactate level in identifying children with mitochondrial disorders. *Eur Radiol* 2017; 27:976–984.
47. Cheong JL, Cady EB, Penrice J, Wyatt JS, Cox IJ, Robertson NJ. Proton MR spectroscopy in neonates with perinatal cerebral hypoxic-ischemic injury: metabolite peak-area ratios, relaxation times, and absolute concentrations. *AJNR Am J Neuroradiol* 2006; 27:1546–1554.
48. Kendall GS, Melbourne A, Johnson S, et al. White matter NAA/Cho and Cho/Cr ratios at MR spectroscopy are predictive of motor outcome in preterm infants. *Radiology* 2014; 271:230–238.
49. Lally PJ, Montaldo P, Oliveira V, et al. MARBLE consortium. Magnetic resonance spectroscopy assessment of brain injury after moderate hypothermia in neonatal encephalopathy: a prospective multicentre cohort study. *Lancet Neurol* 2019; 18:35–45.
50. Kaiser LG, Young K, Matson GB. Numerical simulations of localized high field 1H MR spectroscopy. *J Magn Reson* 2008; 195:67–75.
51. Ganji SK, Banerjee A, Patel AM, et al. T2 measurement of J-coupled metabolites in the human brain at 3T. *NMR Biomed* 2012; 25:523–529.
52. Ross BD, Radda GK, Gadian DG, Rocker G, Esiri M, Falconer-Smith J. Examination of a case of suspected McArdle's syndrome by 31P nuclear magnetic resonance. *N Engl J Med* 1981; 304:1338–1342.

53. Chance B, Eleff S, Leigh JS, Sokolow D, Sapega A. Mitochondrial regulation of phosphocreatine/inorganic phosphate ratios in exercising human muscle: a gated ^{31}P NMR study. *Proc Natl Acad Sci U S A* 1981; 78:6714–6718.
54. in 't Zandt H, van Der Graaf M, Heerschap A. Common processing of in vivo MR spectra. *NMR Biomed* 2001; 14:224–232.
55. Henning A, Fuchs A, Murdoch JB, Boesiger P. Slice-selective FID acquisition, localized by outer volume suppression (FIDLOVS) for (1) H-MRSI of the human brain at 7 T with minimal signal loss. *NMR Biomed* 2009; 22:683–696.
56. Maudsley AA, Govind V, Saigal G, Gold SG, Harris L, Sheriff S. Longitudinal MR Spectroscopy Shows Altered Metabolism in Traumatic Brain Injury. *J Neuroimaging* 2017; 27:562–569.
57. Nassirpour S, Chang P, Henning A. High and ultra-high resolution metabolite mapping of the human brain using ^1H FID MRSI at 9.4T. *Neuroimage* 2018; 168:211–221.
58. Hangel G, Strasser B, Považan M, et al. Ultra-high resolution brain metabolite mapping at 7 T by short-TR Hadamard-encoded FID-MRSI. *Neuroimage* 2018; 168:199–210.
59. Nassirpour S, Chang P, Avdievitch N, Henning A. Compressed sensing for high-resolution nonlipid suppressed ^1H FID MRSI of the human brain at 9.4T. *Magn Reson Med* 2018; 80:2311–2325.
60. Bund C, Lefebvre F, Schott R, et al. Pre- and post-surgery MRSI predictive value in adult oligodendroglioma prognosis. *Magn Reson Imaging* 2018; 52:75–83.
61. Maudsley AA, Andronesi OC, Barker PB, et al. Advanced magnetic resonance spectroscopic neuroimaging: Experts' consensus recommendations. *NMR Biomed* 2021; 34:e4309.
62. Frahm J, Bruhn H, Gyngell ML, Merboldt KD, Hänicke W, Sauter R. Localized high-resolution proton NMR spectroscopy using stimulated echoes: initial applications to human brain in vivo. *Magn Reson Med* 1989; 9:79–93.
63. Alger JR, Sillerud LO, Behar KL, et al. In vivo carbon-13 nuclear magnetic resonance studies of mammals. *Science* 1981; 214:660–662.
64. Bottomley PA, Foster TB, Darrow RD. Depth-resolved surface coil spectroscopy (DRESS) for in vivo ^1H , ^{31}P and ^{13}C NMR. *J Magn Reson Imaging*. 1984; 59:338–342.
65. Bottomley PA, Drayer BP, Smith LS. Chronic adult cerebral infarction studied by phosphorus NMR spectroscopy. *Radiology* 1986; 160:763–766.
66. Scheuermann-Freestone M, Madsen PL, Manners D, et al. Abnormal cardiac and skeletal muscle energy metabolism in patients with type 2 diabetes. *Circulation* 2003; 107:3040–3046.
67. Tomiyasu M, Obata T, Nishi Y, et al. Monitoring of liver glycogen synthesis in diabetic patients using carbon-13 MR spectroscopy. *Eur J Radiol* 2010; 73:300–304.
68. Tkáč I, Deelchand D, Dreher W, et al. Water and lipid suppression techniques for advanced ^1H MRS and MRSI of the human brain: Experts' consensus recommendations. *NMR Biomed* 2021; 34:e4459.
69. Haase A, Frahm J, Hänicke W, Matthaei D. ^1H NMR chemical shift selective (CHESS) imaging. *Phys Med Biol* 1985; 30:341–344.
70. Moonen CTW, Van Zijl PCM. Highly effective water suppression for in vivo proton NMR spectroscopy (DRYSTEAM). *J Magn Reson* 1990; 88:28–41.
71. Klose U. In vivo proton spectroscopy in presence of eddy currents. *Magn Reson Med* 1990; 14:26–30.
72. Doddrell DD, Galloway GJ, Brooks WM, et al. The utilization of two frequency-shifted sinc pulses for performing volume-selected in vivo NMR spectroscopy. *Magn Reson Med* 1986; 3:970–975.
73. Tran TK, Vigneron DB, Sailasuta N, et al. Very selective suppression pulses for clinical MRSI studies of brain and prostate cancer. *Magn Reson Med* 2000; 43:23–33.
74. Choi IY, Tkáč I, Gruetter R. Single-shot, three-dimensional “non-echo” localization method for in vivo NMR spectroscopy. *Magn Reson Med* 2000; 44:387–394.
75. Hahn EL. Spin echoes. *Phys Rev* 1950; 80:580–594.
76. McRobbie D, Moore EA, Graves MJ, Prince MR. The parallel universe: parallel imaging and novel imaging techniques. In: *MRI from picture to proton*, 3rd ed. New York: Cambridge University Press, 2017; 225–250.
77. Schar M, Strasser B, Dydak U. Chemical shift imaging with phase and sensitivity encoding. In: *Handbook of magnetic resonance spectroscopy in vivo*, 1st ed. Chichester: Wiley, 2016; 121–139.
78. LCModel. <http://s-provencher.com/lcmodel.shtml>. (Accessed: November 14, 2021)
79. Provencher SW. Estimation of metabolite concentrations from localized in vivo proton NMR spectra. *Magn Reson Med* 1993; 30:672–679.
80. jMRUI. <http://www.jmrui.eu/welcome-to-the-new-mrui-website/>. (Accessed: May 29, 2021)
81. Jabłoński M, Starčuková J, Starčuk Z. Processing tracking in jMRUI software for magnetic resonance spectra quantitation reproducibility assurance. *BMC Bioinformatics* 2017; 18:56.
82. Tarquin. <http://tarquin.sourceforge.net/index.php>. (Accessed: November 14, 2021)
83. Wilson M, Reynolds G, Kauppinen RA, Arvanitis TN, Peet AC. A constrained least-squares approach to the automated quantitation of in vivo ^1H magnetic resonance spectroscopy data. *Magn Reson Med* 2011; 65:1–12.
84. Poulet JB, Sima DM, Van Huffel S. MRS signal quantitation: a review of time- and frequency-domain methods. *J Magn Reson* 2008; 195:134–144.
85. Wilson M. Adaptive baseline fitting for ^1H MR spectroscopy analysis. *Magn Reson Med* 2021; 85:13–29.
86. Lutkenhoff ES, van Erp TG, Thomas MA, et al. Proton MRS in twin pairs discordant for schizophrenia. *Mol Psychiatry* 2010; 15:308–318.
87. Aoki Y, Abe O, Yahata N, et al. Absence of age-related prefrontal NAA change in adults with autism spectrum disorders. *Transl Psychiatry* 2012; 2:e178.
88. Chang L, Ernst T, Poland RE, Jenden DJ. In vivo proton magnetic resonance spectroscopy of the normal aging human brain. *Life Sci* 1996; 58:2049–2056.
89. Williams LA, Gelman N, Picot PA, et al. Neonatal brain: regional variability of in vivo MR imaging relaxation rates at 3.0 T—initial experience. *Radiology* 2005; 235:595–603.

90. Gwan K, Edzes HT. Water in brain edema. Observations by the pulsed nuclear magnetic resonance technique. *Arch Neurol* 1975; 32:462–465.
91. Just M, Thelen M. Tissue characterization with T1, T2, and proton density values: results in 160 patients with brain tumors. *Radiology* 1988; 169:779–785.
92. Laule C, Vavasour IM, Moore GR, et al. Water content and myelin water fraction in multiple sclerosis. A T2 relaxation study. *J Neurol* 2004; 251:284–293.
93. Frahm J, Bruhn H, Gyngell ML, Merboldt KD, Hänicke W, Sauter R. Localized proton NMR spectroscopy in different regions of the human brain in vivo. Relaxation times and concentrations of cerebral metabolites. *Magn Reson Med* 1989; 11:47–63.
94. Christiansen P, Toft P, Larsson HB, Stubgaard M, Henriksen O. The concentration of N-acetyl aspartate, creatine + phosphocreatine, and choline in different parts of the brain in adulthood and senium. *Magn Reson Imaging* 1993; 11:799–806.
95. Manton DJ, Lowry M, Blackband SJ, Horsman A. Determination of proton metabolite concentrations and relaxation parameters in normal human brain and intracranial tumours. *NMR Biomed* 1995; 8:104–112.
96. Ethofer T, Mader I, Seeger U, et al. Comparison of longitudinal metabolite relaxation times in different regions of the human brain at 1.5 and 3 Tesla. *Magn Reson Med* 2003; 50:1296–1301.
97. Ernst T, Kreis R, Ross BD. Absolute Quantitation of Water and Metabolites in the Human Brain. I. Compartments and Water. *J Magn Reson, Series B* 1993; 102:1–8.
98. Michaelis T, Merboldt KD, Bruhn H, Hänicke W, Frahm J. Absolute concentrations of metabolites in the adult human brain in vivo: quantification of localized proton MR spectra. *Radiology* 1993; 187:219–227.
99. Mekle R, Mlynárik V, Gambarota G, Hergt M, Krueger G, Gruetter R. MR spectroscopy of the human brain with enhanced signal intensity at ultrashort echo times on a clinical platform at 3T and 7T. *Magn Reson Med* 2009; 61:1279–1285.
100. Marjańska M, Auerbach EJ, Valabrègue R, Van de Moortele PF, Adriany G, Garwood M. Localized 1H NMR spectroscopy in different regions of human brain in vivo at 7 T: T2 relaxation times and concentrations of cerebral metabolites. *NMR Biomed* 2012; 25:332–339.
101. Považan M, Strasser B, Hangel G, et al. Simultaneous mapping of metabolites and individual macromolecular components via ultra-short acquisition delay 1 H MRSI in the brain at 7T. *Magn Reson Med* 2018; 79:1231–1240.
102. Giapitzakis IA, Avdievich N, Henning A. Characterization of macromolecular baseline of human brain using metabolite cycled semi-LASER at 9.4T. *Magn Reson Med* 2018; 80:462–473.
103. Lange T, Dydak U, Roberts TP, Rowley HA, Bjeljac M, Boesiger P. Pitfalls in lactate measurements at 3T. *AJNR Am J Neuroradiol* 2006; 27:895–901.
104. Simpson R, Devenyi GA, Jezzard P, Hennessy TJ, Near J. Advanced processing and simulation of MRS data using the FID appliance (FID-A)-An open source, MATLAB-based toolkit. *Magn Reson Med* 2017; 77:23–33.
105. Oz G, Alger JR, Barker PB, et al. MRS Consensus Group. Clinical proton MR spectroscopy in central nervous system disorders. *Radiology* 2014; 270:658–679.
106. Wilson M, Andronesi O, Barker PB, et al. Methodological consensus on clinical proton MRS of the brain: Review and recommendations. *Magn Reson Med* 2019; 82:527–550.
107. Astrakas LG, Argyropoulou MI. Key concepts in MR spectroscopy and practical approaches to gaining biochemical information in children. *Pediatr Radiol* 2016; 46:941–951.
108. Pouwels PJ, Frahm J. Regional metabolite concentrations in human brain as determined by quantitative localized proton MRS. *Magn Reson Med* 1998; 39:53–60.
109. Haga KK, Khor YP, Farrall A, Wardlaw JM. A systematic review of brain metabolite changes, measured with 1H magnetic resonance spectroscopy, in healthy aging. *Neurobiol Aging* 2009; 30:353–363.
110. Cleeland C, Pipingas A, Scholey A, White D. Neurochemical changes in the aging brain: A systematic review. *Neurosci Biobehav Rev* 2019; 98:306–319.
111. Herminghaus S, Dierks T, Pilatus U, et al. Determination of histopathological tumor grade in neuroepithelial brain tumors by using spectral pattern analysis of in vivo spectroscopic data. *J Neurosurg* 2003; 98:74–81.
112. Sankar T, Caramanos Z, Assina R, et al. Prospective serial proton MR spectroscopic assessment of response to tamoxifen for recurrent malignant glioma. *J Neurooncol* 2008; 90:63–76.
113. Opstad KS, Murphy MM, Wilkins PR, Bell BA, Griffiths JR, Howe FA. Differentiation of metastases from high-grade gliomas using short echo time 1H spectroscopy. *J Magn Reson Imaging* 2004; 20:187–192.
114. Majós C, Alonso J, Aguilera C, et al. Proton magnetic resonance spectroscopy ((1)H MRS) of human brain tumours: assessment of differences between tumour types and its applicability in brain tumour categorization. *Eur Radiol* 2003; 13:582–591.
115. Mishra AM, Gupta RK, Jaggi RS, et al. Role of diffusion-weighted imaging and in vivo proton magnetic resonance spectroscopy in the differential diagnosis of ring-enhancing intracranial cystic mass lesions. *J Comput Assist Tomogr* 2004; 28:540–547.
116. Kim H, Thompson RB, Hanstock CC, Allen PS. Variability of metabolite yield using STEAM or PRESS sequences in vivo at 3.0 T, illustrated with myo-inositol. *Magn Reson Med* 2005; 53:760–769.
117. Branzoli F, Di Stefano AL, Capelle L, et al. Highly specific determination of IDH status using edited in vivo magnetic resonance spectroscopy. *Neuro Oncol* 2018; 20:907–916.
118. Andronesi OC, Kim GS, Gerstner E, et al. Detection of 2-hydroxyglutarate in IDH-mutated glioma patients by in vivo spectral-editing and 2D correlation magnetic resonance spectroscopy. *Sci Transl Med* 2012; 4:116ra4.
119. Kim S, Salamon N, Jackson HA, Blüml S, Panigrahy A. PET imaging in pediatric neuroradiology: current and future applications. *Pediatr Radiol* 2010; 40:82–96.
120. Nguyen TB, Melkus G, Taccone M, et al. Preoperative Determination of Isocitrate Dehydrogenase Mutation in

- Gliomas Using Spectral Editing MRS: A Prospective Study. *J Magn Reson Imaging* 2021; 53:416–426.
121. Shonk TK, Moats RA, Gifford P, et al. Probable Alzheimer disease: diagnosis with proton MR spectroscopy. *Radiology* 1995; 195:65–72.
 122. Dixon RM, Bradley KM, Budge MM, Styles P, Smith AD. Longitudinal quantitative proton magnetic resonance spectroscopy of the hippocampus in Alzheimer's disease. *Brain* 2002; 125:2332–2341.
 123. Fayed N, Dávila J, Oliveros A, Castillo J, Medrano JJ. Utility of different MR modalities in mild cognitive impairment and its use as a predictor of conversion to probable dementia. *Acad Radiol* 2008; 15:1089–1098.
 124. Henigsberg N, Kalember P, Hrabac P, et al. 1-H MRS changes in dorsolateral prefrontal cortex after donepezil treatment in patients with mild to moderate Alzheimer's disease. *Coll Antropol* 2011; 35 Suppl 1:159–162.
 125. Modrego PJ, Fayed N, Errea JM, Rios C, Pina MA, Sarasa M. Memantine versus donepezil in mild to moderate Alzheimer's disease: a randomized trial with magnetic resonance spectroscopy. *Eur J Neurol* 2010; 17:405–412.
 126. Sijens PE, Verbruggen KT, Meiners LC, Soorani-Luning RJ, Rake JP, Oudkerk M. 1H chemical shift imaging of the brain in guanidino methyltransferase deficiency, a creatine deficiency syndrome; guanidinoacetate accumulation in the gray matter. *Eur Radiol* 2005; 15:1923–1926.
 127. Sijens PE, Verbruggen KT, Oudkerk M, van Spronsen FJ, Soorani-Luning RJ. 1H MR spectroscopy of the brain in Cr transporter defect. *Mol Genet Metab* 2005; 86:421–422.
 128. Battini R, Leuzzi V, Carducci C, et al. Creatine depletion in a new case with AGAT deficiency: clinical and genetic study in a large pedigree. *Mol Genet Metab* 2002; 77:326–331.
 129. Gripp KW, Zimmerman RA, Wang ZJ, et al. Imaging studies in a unique familial dysmyelinating disorder. *AJNR Am J Neuroradiol* 1998; 19:1368–1372.
 130. Varho T, Komu M, Sonninen P, et al. A new metabolite contributing to N-acetyl signal in 1H MRS of the brain in Salla disease. *Neurology* 1999; 52:1668–1672.
 131. Willemsen MA, Van Der Graaf M, Van Der Knaap MS, et al. MR imaging and proton MR spectroscopic studies in Sjögren-Larsson syndrome: characterization of the leukoencephalopathy. *AJNR Am J Neuroradiol* 2004; 25:649–657.
 132. Brockmann K, Bjornstad A, Dechent P, et al. Succinate in dystrophic white matter: a proton magnetic resonance spectroscopy finding characteristic for complex II deficiency. *Ann Neurol* 2002; 52:38–46.
 133. Jan W, Zimmerman RA, Wang ZJ, Berry GT, Kaplan PB, Kaye EM. MR diffusion imaging and MR spectroscopy of maple syrup urine disease during acute metabolic decompensation. *Neuroradiology* 2003; 45:393–399.
 134. Otaduy MC, Leite CC, Lacerda MT, et al. Proton MR spectroscopy and imaging of a galactosemic patient before and after dietary treatment. *AJNR Am J Neuroradiol* 2006; 27:204–207.
 135. Huisman TA, Thiel T, Steinmann B, Zeilinger G, Martin E. Proton magnetic resonance spectroscopy of the brain of a neonate with nonketotic hyperglycinemia: in vivo-
in vitro (ex vivo) correlation. *Eur Radiol* 2002; 12:858–861.
 136. Huck JH, Verhoeven NM, Struys EA, Salomons GS, Jakobs C, van der Knaap MS. Ribose-5-phosphate isomerase deficiency: new inborn error in the pentose phosphate pathway associated with a slowly progressive leukoencephalopathy. *Am J Hum Genet* 2004; 74:745–751.
 137. Wilken B, Dechent P, Hanefeld F, Frahm J. Proton MRS of a child with Sandhoff disease reveals elevated brain hexosamine. *Eur J Paediatr Neurol* 2008; 12:56–60.
 138. Yalçinkaya C, Dinçer A, Gündüz E, Fiçicioglu C, Koçer N, Aydın A. MRI and MRS in HMG-CoA lyase deficiency. *Pediatr Neurol* 1999; 20:375–380.
 139. Aoki Y, Watanabe T, Abe O, et al. Oxytocin's neurochemical effects in the medial prefrontal cortex underlie recovery of task-specific brain activity in autism: a randomized controlled trial. *Mol Psychiatry* 2015; 20:447–453.
 140. Bustillo JR, Rowland LM, Jung R, et al. Proton magnetic resonance spectroscopy during initial treatment with antipsychotic medication in schizophrenia. *Neuropsychopharmacology* 2008; 33:2456–2466.
 141. Molina V, Sánchez J, Sanz J, et al. Dorsolateral prefrontal N-acetyl-aspartate concentration in male patients with chronic schizophrenia and with chronic bipolar disorder. *Eur Psychiatry* 2007; 22:505–512.
 142. Gabbay V, Hess DA, Liu S, Babb JS, Klein RG, Gonen O. Lateralized caudate metabolic abnormalities in adolescent major depressive disorder: a proton MR spectroscopy study. *Am J Psychiatry* 2007; 164:1881–1889.
 143. Auer DP, Pütz B, Kraft E, Lipinski B, Schill J, Holsboer F. Reduced glutamate in the anterior cingulate cortex in depression: an in vivo proton magnetic resonance spectroscopy study. *Biol Psychiatry* 2000; 47:305–313.
 144. Bhagwagar Z, Wylezinska M, Jezard P, et al. Reduction in occipital cortex gamma-aminobutyric acid concentrations in medication-free recovered unipolar depressed and bipolar subjects. *Biol Psychiatry* 2007; 61:806–812.
 145. Olvera RL, Caetano SC, Fonseca M, et al. Low levels of N-acetyl aspartate in the left dorsolateral prefrontal cortex of pediatric bipolar patients. *J Child Adolesc Psychopharmacol* 2007; 17:461–473.
 146. Rovira A, León A. MR in the diagnosis and monitoring of multiple sclerosis: an overview. *Eur J Radiol* 2008; 67:409–414.
 147. Cianfoni A, Niku S, Imbesi SG. Metabolite findings in tumefactive demyelinating lesions utilizing short echo time proton magnetic resonance spectroscopy. *AJNR Am J Neuroradiol* 2007; 28:272–277.
 148. Khan O, Shen Y, Bao F, et al. Long-term study of brain 1H-MRS study in multiple sclerosis: effect of glatiramer acetate therapy on axonal metabolic function and feasibility of long-term H-MRS monitoring in multiple sclerosis. *J Neuroimaging* 2008; 18:314–319.
 149. Wattjes MP, Harzheim M, Lutterbey GG, Klotz L, Schild HH, Träber F. Axonal damage but no increased glial cell activity in the normal-appearing white matter of patients with clinically isolated syndromes suggestive of multiple sclerosis using high-field magnetic resonance spectroscopy. *AJNR Am J Neuroradiol* 2007; 28:1517–1522.

150. Summers M, Swanton J, Fernando K, et al. Cognitive impairment in multiple sclerosis can be predicted by imaging early in the disease. *J Neurol Neurosurg Psychiatry* 2008; 79:955–958.
151. Duan Y, Liu Z, Liu Y, et al. Metabolic changes in normal-appearing white matter in patients with neuromyelitis optica and multiple sclerosis: a comparative magnetic resonance spectroscopy study. *Acta Radiol* 2017; 58:1132–1137.
152. Nicoli F, Lefur Y, Denis B, Ranjeva JP, Confort-Gouny S, Cozzone PJ. Metabolic counterpart of decreased apparent diffusion coefficient during hyperacute ischemic stroke: a brain proton magnetic resonance spectroscopic imaging study. *Stroke* 2003; 34:e82–87.
153. Stengel A, Neumann-Haefelin T, Singer OC, et al. Multiple spin-echo spectroscopic imaging for rapid quantitative assessment of N-acetylaspartate and lactate in acute stroke. *Magn Reson Med* 2004; 52:228–238.
154. Dani KA, An L, Henning EC, Shen J, Warach S; National Institute of Neurological Disorders and Stroke Natural History of Stroke Investigators. Multivoxel MR spectroscopy in acute ischemic stroke: comparison to the stroke protocol MRI. *Stroke* 2012; 43:2962–2967.
155. Abragam A. Principles of nuclear magnetism. New York: Oxford University Press, 1983; 648.
156. Konstantin S, Nagel AM. Measurement techniques for magnetic resonance imaging of fast relaxing nuclei. *MAGMA* 2014; 27:5–19.
157. Bogner W, Otazo R, Henning A. Accelerated MR spectroscopic imaging—a review of current and emerging techniques. *NMR Biomed* 2020; e4314.
158. Takeda K, Ichijo N, Noda Y, Takegoshi K. Elemental analysis by NMR. *J Magn Reson* 2012; 224:48–52.
159. Watanabe H, Umeda M, Ishihara Y, et al. Human brain glucose metabolism mapping using multislice 2D (1)H-(13)C correlation HSQC spectroscopy. *Magn Reson Med* 2000; 43:525–533.
160. Beckmann N, Fried R, Turkalj I, Seelig J, Keller U, Stalder G. Noninvasive observation of hepatic glycogen formation in man by 13C MRS after oral and intravenous glucose administration. *Magn Reson Med* 1993; 29:583–590.
161. Chen W, Zhu XH, Gruetter R, Seaquist ER, Adriany G, Ugurbil K. Study of tricarboxylic acid cycle flux changes in human visual cortex during hemifield visual stimulation using (1)H-[(13)C] MRS and fMRI. *Magn Reson Med* 2001; 45:349–355.
162. Chen W, Zhu X, Ugurbil K. Imaging cerebral metabolic rate of oxygen consumption (CMRO₂) using ¹⁷O NMR approach at ultrahigh field. In: Shulman RG, Rothman DL., et al. *Brain energetics & neuronal activity*. Chichester: John Wiley & Sons; 2005; 125–146.
163. Mason GF, Petersen KF, de Graaf RA, Shulman GI, Rothman DL. Measurements of the anaplerotic rate in the human cerebral cortex using 13C magnetic resonance spectroscopy and [1-13C] and [2-13C] glucose. *J Neurochem* 2007; 100:73–86.
164. Bowers CR, Weitekamp DP. Transformation of symmetrization order to nuclear-spin magnetization by chemical reaction and nuclear magnetic resonance. *Phys Rev Lett* 1986; 57:2645–2648.
165. Ardenkjaer-Larsen JH, Fridlund B, Gram A, et al. Increase in signal-to-noise ratio of > 10,000 times in liquid-state NMR. *Proc Natl Acad Sci U S A* 2003; 100:10158–10163.
166. Wang ZJ, Ohliger MA, Larson PEZ, et al. Hyperpolarized 13C MRI: State of the Art and Future Directions. *Radiology* 2019; 291:273–284.
167. Nelson SJ, Kurhanewicz J, Vigneron DB, et al. Metabolic imaging of patients with prostate cancer using hyperpolarized [1-¹³C]pyruvate. *Sci Transl Med* 2013; 5:198ra108.
168. Miloshev VZ, Granlund KL, Boltyanskiy R, et al. Metabolic Imaging of the Human Brain with Hyperpolarized 13C Pyruvate Demonstrates 13C Lactate Production in Brain Tumor Patients. *Cancer Res* 2018; 78:3755–3760.
169. Park I, Larson PEZ, Gordon JW, et al. Development of methods and feasibility of using hyperpolarized carbon-13 imaging data for evaluating brain metabolism in patient studies. *Magn Reson Med* 2018; 80:864–873.
170. Park JM, Josan S, Grafendorfer T, et al. Measuring mitochondrial metabolism in rat brain in vivo using MR Spectroscopy of hyperpolarized [2-¹³C]pyruvate. *NMR Biomed* 2013; 26:1197–1203.
171. Josan S, Hurd R, Park JM, et al. Dynamic metabolic imaging of hyperpolarized [2-(13) C]pyruvate using spiral chemical shift imaging with alternating spectral band excitation. *Magn Reson Med* 2014; 71:2051–2058.
172. Mignion L, Dutta P, Martinez GV, Foroutan P, Gillies RJ, Jordan BF. Monitoring chemotherapeutic response by hyperpolarized 13C-fumarate MRS and diffusion MRI. *Cancer Res* 2014; 74:686–694.
173. Chen HY, Larson PEZ, Bok RA, et al. Assessing Prostate Cancer Aggressiveness with Hyperpolarized Dual-Agent 3D Dynamic Imaging of Metabolism and Perfusion. *Cancer Res* 2017; 77:3207–3216.
174. Pekar J, Ligeti L, Ruttner Z, et al. In vivo measurement of cerebral oxygen consumption and blood flow using 17O magnetic resonance imaging. *Magn Reson Med* 1991; 21:313–319.
175. Kwong KK, Hopkins AL, Belliveau JW, et al. Proton NMR imaging of cerebral blood flow using H₂(17)O. *Magn Reson Med* 1991; 22:154–158.
176. Ronen I, Merkle H, Ugurbil K, Navon G. Imaging of H₂17O distribution in the brain of a live rat by using proton-detected 17O MRI. *Proc Natl Acad Sci U S A* 1998; 95:12934–12939.
177. Taylor DR, Baumgardner JE, Regatte RR, Leigh JS, Reddy R. Proton MRI of metabolically produced H₂ 17O using an efficient 17O₂ delivery system. *Neuroimage* 2004; 22:611–618.
178. Zhu XH, Zhang N, Zhang Y, Zhang X, Ugurbil K, Chen W. In vivo 17O NMR approaches for brain study at high field. *NMR Biomed* 2005; 18:83–103.
179. Atkinson IC, Thulborn KR. Feasibility of mapping the tissue mass corrected bioscale of cerebral metabolic rate of oxygen consumption using 17-oxygen and 23-sodium MR imaging in a human brain at 9.4 T. *Neuroimage* 2010; 51:723–733.
180. Zhu XH, Lu M, Chen W. Quantitative imaging of brain energy metabolisms and neuroenergetics using in vivo X-

- nuclear 2H, 17O and 31P MRS at ultra-high field. *J Magn Reson* 2018; 292:155–170.
181. Niesporek SC, Umatham R, Lommen JM, et al. Reproducibility of CMRO2 determination using dynamic 17 O MRI. *Magn Reson Med* 2018; 79:2923–2934.
 182. Kudo K, Harada T, Kameda H, et al. Indirect Proton MR Imaging and Kinetic Analysis of 17O-Labeled Water Tracer in the Brain. *Magn Reson Med Sci* 2018; 17:223–230.
 183. Elliott SJ, Bengs C, Kouril K, et al. NMR Lineshapes and Scalar Relaxation of the Water-Endofullerene H217 O@C60. *Chemphyschem* 2018; 19:251–255.
 184. Meiboom S. Nuclear magnetic resonance study of the proton transfer in water. *J Chem Phys* 1961; 34:375–388.
 185. Hopkins AL, Barr RG. Oxygen-17 compounds as potential NMR T2 contrast agents: enrichment effects of H2(17)O on protein solutions and living tissues. *Magn Reson Med* 1987; 4:399–403.
 186. Yeung HN, Lent AH. Proton transverse relaxation rate of 17O-enriched water. *Magn Reson Med* 1987; 5:87–92.
 187. Kwong KK, Xiong J, Kuan WP, Cheng HM. Measurement of water movement in the rabbit eye in vivo using H2(17)O. *Magn Reson Med* 1991; 22:443–450.
 188. Leslie TK, James AD, Zaccagna F, et al. Sodium homeostasis in the tumour microenvironment. *Biochim Biophys Acta Rev Cancer* 2019; 1872:188304.
 189. Poku LO, Phil M, Cheng Y, Wang K, Sun X. 23 Na-MRI as a Noninvasive Biomarker for Cancer Diagnosis and Prognosis. *J Magn Reson Imaging* 2021; 53:995–1014.
 190. Ouwerkerk R, Bleich KB, Gillen JS, Pomper MG, Bottomley PA. Tissue sodium concentration in human brain tumors as measured with 23Na MR imaging. *Radiology* 2003; 227:529–537.
 191. Ouwerkerk R, Jacobs MA, Macura KJ, et al. Elevated tissue sodium concentration in malignant breast lesions detected with non-invasive 23Na MRI. *Breast Cancer Res Treat* 2007; 106:151–160.
 192. Jacobs MA, Stearns V, Wolff AC, et al. Multiparametric magnetic resonance imaging, spectroscopy and multinuclear (²³Na) imaging monitoring of preoperative chemotherapy for locally advanced breast cancer. *Acad Radiol* 2010; 17:1477–1485.
 193. Jacobs MA, Ouwerkerk R, Wolff AC, et al. Monitoring of neoadjuvant chemotherapy using multiparametric, ²³Na sodium MR, and multimodality (PET/CT/MRI) imaging in locally advanced breast cancer. *Breast Cancer Res Treat* 2011; 128:119–126.
 194. Broeke NC, Peterson J, Lee J, et al. Characterization of clinical human prostate cancer lesions using 3.0-T sodium MRI registered to Gleason-graded whole-mount histopathology. *J Magn Reson Imaging* 2019; 49:1409–1419.
 195. Deen SS, Riemer F, McLean MA, et al. Sodium MRI with 3D-cones as a measure of tumour cellularity in high grade serous ovarian cancer. *Eur J Radiol Open* 2019; 6:156–162.
 196. Barrett T, Riemer F, McLean MA, et al. Molecular imaging of the prostate: Comparing total sodium concentration quantification in prostate cancer and normal tissue using dedicated 13 C and 23 Na endorectal coils. *J Magn Reson Imaging* 2020; 51:90–97.
 197. Oberhaensli RD, Galloway GJ, Taylor DJ, Bore PJ, Radda GK. Assessment of human liver metabolism by phosphorus-31 magnetic resonance spectroscopy. *Br J Radiol* 1986; 59:695–699.
 198. Liu Y, Gu Y, Yu X. Assessing tissue metabolism by phosphorous-31 magnetic resonance spectroscopy and imaging: a methodology review. *Quant Imaging Med Surg* 2017; 7:707–726.
 199. Griffiths JR, Cady E, Edwards RH, McCready VR, Wilkie DR, Wiltshaw E. 31P-NMR studies of a human tumour in situ. *Lancet* 1983; 1:1435–1436.
 200. Evanochko WT, Sakai TT, Ng TC, et al. NMR study of in vivo RIF-1 tumors. Analysis of perchloric acid extracts and identification of 1H, 31P and 13C resonances. *Biochim Biophys Acta* 1984; 805:104–116.
 201. Eliyahu G, Kreizman T, Degani H. Phosphocholine as a biomarker of breast cancer: molecular and biochemical studies. *Int J Cancer* 2007; 120:1721–1730.